Secrecy Performance Analysis for Water-to-Air Visible Light Communication

Qingqing Hu, Chen Gong, *Senior Member, IEEE*, Tianrui Lin, Jianghua Luo, and Zhengyuan Xu, *Senior Member, IEEE*

***Abstract*—This paper investigates the physical-layer security for water-to-air (W2A) visible light communication (VLC). The impacts of surface fluctuation and underwater scattering on the channel gain are theoretically analyzed, which is verified in a laboratory W2A-VLC link. The statistical properties of wave slope under experimental conditions are measured by image processing and the probability density function of the slope can be approximated by a logistic distribution. We observe that dynamic waves can cause information leakage and experimental results indicate that the probability of secure communication increases from 90.39% to 96.18% as the eavesdropper's elevation increases from 1.15 m to 1.42 m, which are approximately consistent with the numerical results. To investigate the parameters affecting the secrecy performance, several secrecy performance metrics are numerically calculated under different wave intensities, eavesdropper's locations, divergence angles of LED, underwater scattering coefficients and wavelengths of transmitted beam. It is seen that the secrecy performance is degraded as the wave intensity increases, while random scattering can mitigate the water surface fluctuations and reduce the probability of information leakage.**

***Index Terms*—Scattering, secrecy performance, surface fluctuation, visible light communication, water-to-air.**

I. Introduction

NOWADAYS, there has been a growing interest in the ocean exploration and thus underwater wireless communication technology has attracted extensive attention [1]. Several wireless carriers can be adopted to transmit data in the underwater environment. However, radio-frequency (RF) waves are heavily attenuated by sea water due to the skin effect [2] and acoustic communication systems suffer from low data rates and high latencies. Therefore, underwater optical wireless communication has become an attractive and viable alternative, since it can provide a much higher transmission bandwidth and much higher data rate under short-to-medium distance [3].

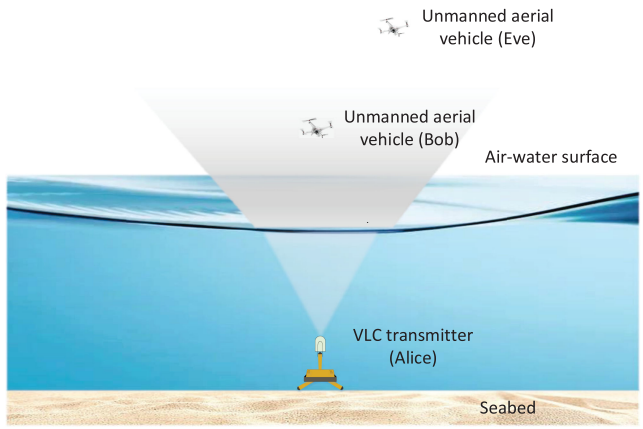

Fig. 1. A W2A-VLC scenario with eavesdropper.

Due to inherent broadcast nature of visible light communication (VLC) channels, the information may be eavesdropped by unauthorized terminals in the coverage of the light-emitting diode (LED) [4]. In indoor scenarios, the secrecy performance has been investigated for the case of randomly located eavesdroppers [5], [6]. The upper and lower bounds on the secrecy capacity were derived with both average and peak optical intensity constraints [7], [8]. Robust beamforming and jamming signal schemes have been widely adopted to improve the secrecy performance [9]–[12]. In outdoor scenarios, the impact of link misalignment on secure communication was theoretically analyzed by modeling the misalignment as a four-parameter Beckmann distribution [13], [14]. The probability of secure communication was studied via considering random fading characteristic of the received optical intensity caused by the atmospheric turbulence [15], [16]. To the best of the authors' knowledge, the secrecy performance for W2A-VLC scenario has not been systematically investigated in previous studies.

In this work, we consider the impacts of fluctuation and refraction of water surface and underwater scattering on secrecy performance. A typical W2A-VLC scenario is shown in Fig. 1, where a underwater platform (Alice) transmits information to an unmanned aerial vehicle (Bob) in the presence of an unmanned aerial vehicle (Eve) eavesdropping the information. Considering

Manuscript received November 13, 2021; revised February 7, 2022 and March 15, 2022; accepted April 13, 2022. Date of publication April 19, 2022; date of current version July 16, 2022. This work was supported in part by the National Key Research and Development Program of China under Grant 2018YFB1801904, in part by the Key Program of National Natural Science Foundation of China under Grant 61631018, in part by the National Natural Science Foundation of China under Grants 62171428 and 62101526, and in part by the Key Research Program of Frontier Sciences of CAS under Grant QYZDY-SSW-JSC003. *(Corresponding author: Chen Gong.)*

Qingqing Hu, Chen Gong, Tianrui Lin, and Zhengyuan Xu are with the Key Laboratory of Wireless-Optical Communications, Chinese Academy of Sciences, University of Science and Technology of China, Hefei, Anhui 230027, China (e-mail: ruixihu@mail.ustc.edu.cn; cgong821@ustc.edu.cn; trlin@mail.ustc.edu.cn; xuzy@ustc.edu.cn).

Jianghua Luo is with the School of Physics and Optoelectronic Engineering, Yangtze University, Jingzhou 434023, China (e-mail: jhluo@yangtzeu.edu.cn).

Color versions of one or more figures in this article are available at https://doi.org/10.1109/JLT.2022.3168258.

Digital Object Identifier 10.1109/JLT.2022.3168258

low-cost LEDs adopted in the transmitter, which usually have a large coverage area, the effect of blockage caused by Bob can be negligible. Due to the massive scattering particles in the water, the beam has larger divergence and coverage area. Besides, the wavy surface caused by water turbulence and wind is considered, resulting in a random deflection of the light beam. Therefore, Eve may have a chance to eavesdrop a portion of the power emitted by Alice, threatening the communication security. Since the transmitter is several meters under the water surface, the temperature and salinity difference caused by the turbulence is negligible, where the main effect of turbulence is the wavy water surface [17]. Moreover, the temporal dispersion caused by scattering can be neglected if the transmission speed is lower than Gbps [2], which is the application scenario of this work. The motivation of this paper is to investigate the secrecy performance of W2A-VLC systems. Firstly, channel gains from Alice to Bob and Eve in the presence of surface fluctuation and underwater scattering are theoretically derived. A real W2A-VLC link is established to verify the theoretical derivation and explore the secrecy performance under the wavy surface. The experimental results show the probability of secure communication increases from 90.39% to 96.18% as the eavesdropper's elevation increases from 1.15 m to 1.42 m, which is approximately consistent with the numerical results. The wave slope statistics under the experimental condition are measured and characterized through image processing. Then, we investigate the secrecy performance via numerical simulations for a wider range of parameters. The intensity distributions on receiving plane, channel gain distributions and correlation coefficients are investigated under wavy surface conditions. In addition, secrecy performance metrics including insecure region, probability of strictly positive secrecy capacity (SPSC) and secrecy outage probability (SOP) are investigated in the numerical calculation. It is seen that secrecy performance improves as Eve's distance increases and the wave intensity decreases. While random scattering can reduce the effect of waves, and thus a type of water with a larger scattering coefficient and a light beam with a shorter wavelength would increase the probability of secure communication. There exists an optimal divergence angle of LED because too small or too large divergence angle will increase the probability of eavesdropper's channel being better than legitimate receiver's.

The remainder of this paper is organized as follows. In Section II, we theoretically investigate the channel gain from an underwater transmitter to a receiver in the air, considering dynamic water surface fluctuation and underwater scattering. Several secrecy performance metrics including secrecy capacity, probability of SPSC and SOP are introduced. In Section III, a real W2A-VLC system is established to verify the theoretical derivation, and statistical properties of wave slope in the experimental environment are characterized by image processing. In Section IV, we calculate the PDFs of channel gain and correlation coefficients at different positions, investigate the intensity distributions and insecure regions in receiving plane under different types of water surface, and numerically investigate the probability of SPSC and SOP under different parameters, such as wave intensities, scattering coefficients, wavelengths of the beam and divergence angles of LED. Finally, we conclude this work in Section V.

II. System Model and Secrecy Performance Metrics

A. System Model

Consider a W2A-VLC system as shown in Fig. 2. An underwater transmitter Alice modulates information bits to visible light signals and sends them to a legitimate receiver Bob in the air, while an eavesdropper Eve is stealing information in a passive manner. The receiving areas of Bob and Eve are $(x_B \pm d_{xB}, y_B \pm d_{yB}, z_B)$ and $(x_E \pm d_{xE}, y_E \pm d_{yE}, z_E)$, respectively. The underwater transmitter Alice is located at $(0, 0, z_0)$ and sends a visible light beam with divergence half-angle α, source aperture r, zenith angle γ_0 and total power P_t. After propagating up to the air/water surface, one of the rays sent by Alice reaches the surface at $(x_0, y_0, 0)$ with incident angle $\gamma \triangleq \{\gamma_x, \gamma_y\}$ (γ_x and γ_y are the incident angles measured in $x-z$ plane and $y-z$ plane, respectively). The intensity of the incident ray is given by [18],

$$\begin{aligned}&\Delta I\left(x_0, y_0, z_0, \gamma_x, \gamma_y\right)\\&= \frac{P_t}{\left(\pi U_\phi R_1\right)^2} \exp\left\{\begin{array}{l}-a\sqrt{\left({x_0}^2+{y_0}^2+{z_0}^2\right)} - \frac{{\xi_x}^2+{\xi_y}^2}{{R_1}^2} - \\ \frac{1}{{U_\phi}^2}\left[\left(\gamma_x - \bar{\gamma}_x - \frac{\varepsilon_x|x_0|\theta_m}{\sqrt{{x_0}^2+{y_0}^2}}\right)^2 + \right.\\ \left.\left(\gamma_y - \bar{\gamma}_y - \frac{\varepsilon_y|y_0|\theta_m}{\sqrt{{x_0}^2+{y_0}^2}}\right)^2\right]\end{array}\right\},\end{aligned} \tag{1}$$

where

$${U_\phi}^2 = \frac{s}{\delta^2} \times \left[{x_0}^2 + {y_0}^2 + {z_0}^2\right]^{\frac{1}{2}} \times \left[\frac{1+2V+6l+3lV}{2+3l+3V}\right], \tag{2}$$

$${R_1}^2 = \frac{s}{\delta^2} \times \left[{x_0}^2 + {y_0}^2 + {z_0}^2\right]^{\frac{3}{2}} \times \left[\frac{2+3l+3V}{3}\right], \tag{3}$$

$$\theta_m = \frac{3+3V}{2+3l+3V}\left[\frac{\sqrt{{\xi_x}^2+{\xi_y}^2}}{\sqrt{{x_0}^2+{y_0}^2+{z_0}^2}}\right], \tag{4}$$

with

$$V = \frac{\alpha^2\delta^2}{s[{x_0}^2+{y_0}^2+{z_0}^2]^{\frac{1}{2}}}, \tag{5}$$

$$l = \frac{r^2\delta^2}{s[{x_0}^2+{y_0}^2+{z_0}^2]^{\frac{3}{2}}}, \tag{6}$$

$$\xi_x = \left[\arcsin\left(\frac{-x_0}{\sqrt{{x_0}^2+{z_0}^2}}\right) - \bar{\gamma}_x\right] \times \sqrt{{x_0}^2+{z_0}^2}, \tag{7}$$

$$\xi_y = \left[\arcsin\left(\frac{-y_0}{\sqrt{{y_0}^2+{z_0}^2}}\right) - \bar{\gamma}_y\right] \times \sqrt{{y_0}^2+{z_0}^2}, \tag{8}$$

$$\bar{\gamma}_x = \gamma_0, \tag{9}$$

$$\bar{\gamma}_y = 0, \tag{10}$$

$$\varepsilon_x = \mathrm{sign}(\xi_x), \tag{11}$$

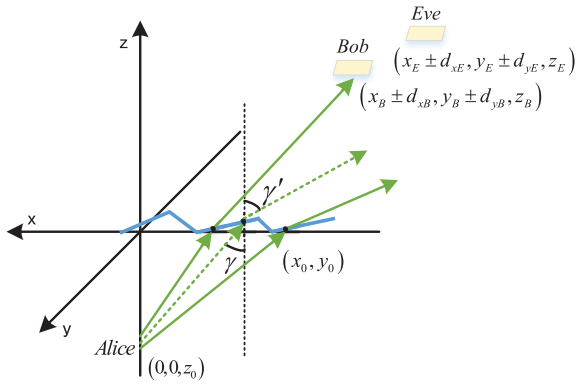

Fig. 2. The coordinate system of W2A-VLC.

$$\varepsilon_y = \text{sign}(\xi_y). \tag{12}$$

In the above Equations, a is absorption coefficient and s is scattering coefficient, and δ is the parameter of normalized scattering function $f(\theta) = \frac{\delta}{2\pi\theta} e^{-\delta\,\theta}$.

B. Channel Gain Characterization

Existing works on W2A-VLC transmission characterization under dynamic water surface with scattering adopted Monte Carlo methods [2], which will consume a lot of computing resources. In (69) of [18], the link loss was theoretically derived in a simplified case where the water surface is calm. In this section, based on the ray intensity in [18], we further derive the channel gain at the receiver for arbitrary wavy surface. To calculate the channel gain, we need to analyze the conditions of rays that can reach the receiving plane. Assume that the refracted ray at surface point (x_0, y_0) has refraction angle $({\gamma'}_x, {\gamma'}_y)$. According to geometric relations, the condition for the refracted ray to reach the receiving plane $(x \pm d_x, y \pm d_y, z)$ is

$$\begin{cases} -z\tan({\gamma'}_x) + x_0 \in [x - d_x, x + d_x] \\ -z\tan({\gamma'}_y) + y_0 \in [y - d_y, y + d_y] \end{cases}. \tag{13}$$

Then, the range of refraction angles is given as follows,

$$\begin{cases} {\gamma'}_x \in \left[\arctan\left(\frac{x+d_x-x_0}{-z}\right), \arctan\left(\frac{x-d_x-x_0}{-z}\right)\right] \\ \quad \triangleq [{\gamma'}_{xL}, {\gamma'}_{xU}] \\ {\gamma'}_y \in \left[\arctan\left(\frac{y+d_y-y_0}{-z}\right), \arctan\left(\frac{y-d_y-y_0}{-z}\right)\right] \\ \quad \triangleq [{\gamma'}_{yL}, {\gamma'}_{yU}] \end{cases}. \tag{14}$$

According to Snell's law, the relationship between incident and refracted rays is given by,

$$n' \sin(\gamma' + R) = n \sin(\gamma + R), \tag{15}$$

where R is the local slope of the air/water surface, n' is the refractive index of air and n is the refractive index of water.

Theorem 1: The range of incident angles is derived from (14), as follows,

$$\begin{cases} \gamma_x \in [\gamma_{xL}, \gamma_{xU}] \\ \gamma_y \in [\gamma_{yL}, \gamma_{yU}] \end{cases}. \tag{16}$$

Proof: See Appendix A and $\gamma_{xL}, \gamma_{xU}, \gamma_{yL}$ and γ_{yU} are shown in the Appendix A.

When $(\gamma' + R) < 45^\circ$, (15) can be approximated as [18],

$$\gamma \approx \frac{n'}{n}\gamma' + \left(\frac{n'}{n} - 1\right) R. \tag{17}$$

Therefore, the range of incident angles can be simplified as,

$$\begin{cases} \gamma_x \in \left[\frac{n'}{n}{\gamma'}_{xL} + \left(\frac{n'}{n} - 1\right) R_x,\ \frac{n'}{n}{\gamma'}_{xU} + \left(\frac{n'}{n} - 1\right) R_x\right] \\ \gamma_y \in \left[\frac{n'}{n}{\gamma'}_{yL} + \left(\frac{n'}{n} - 1\right) R_y,\ \frac{n'}{n}{\gamma'}_{yU} + \left(\frac{n'}{n} - 1\right) R_y\right] \end{cases}. \tag{18}$$

When such incident rays does not exist, for example, the rays do not pass the transmitter, the intensity contribution of the rays becomes zero. Then, received power on the receiving plane $(x \pm d_x, y \pm d_y, z)$ is

$$P = \int_{x_0}\int_{y_0}\int_{\gamma_x}\int_{\gamma_y} \Delta I(x_0, y_0, z_0, \gamma_x, \gamma_y)\, d\gamma_x d\gamma_y dx_0 dy_0, \tag{19}$$

where $(x_0, y_0) \in \Omega$, which is the area of light spot on the water surface. In the following, we provide a general form of link gain, where approximation in (17) does not necessarily hold.

Theorem 2: The channel gain of the receiving plane $(x \pm d_x, y \pm d_y, z)$ can be written in (20), as shown at the bottom of this page, where $erf(x) = \frac{2}{\sqrt{\pi}} \int_0^x e^{-\eta^2} d\eta$.

Proof: See Appendix B.

The channel gains of Bob and Eve can be obtained by replacing the receiving area from $(x \pm d_x, y \pm d_y, z)$ to $(x_B \pm d_{xB}, y_B \pm d_{yB}, z_B)$ and $(x_E \pm d_{xE}, y_E \pm d_{yE}, z_E)$, respectively.

C. Secrecy Performance Metrics

An achievable secrecy rate is given as follows [19],

$$C_s = \max\{C_B - C_E,\ 0\}, \tag{21}$$

$$h = \int_{x_0}\int_{y_0} \left\{ \begin{array}{l} \frac{1}{4\pi {R_1}^2} \exp\left\{-a\sqrt{({x_0}^2 + {y_0}^2 + {z_0}^2)} - \frac{{\xi_x}^2 + {\xi_y}^2}{{R_1}^2}\right\} \times \\ \left[erf\left(\frac{\gamma_{xU} - \bar{\gamma}_x - \frac{\varepsilon_x |x_0| \theta_m}{\sqrt{{x_0}^2 + {y_0}^2}}}{U_\phi}\right) - erf\left(\frac{\gamma_{xL} - \bar{\gamma}_x - \frac{\varepsilon_x |x_0| \theta_m}{\sqrt{{x_0}^2 + {y_0}^2}}}{U_\phi}\right)\right] \\ \times \left[erf\left(\frac{\gamma_{yU} - \bar{\gamma}_y - \frac{\varepsilon_y |y_0| \theta_m}{\sqrt{{x_0}^2 + {y_0}^2}}}{U_\phi}\right) - erf\left(\frac{\gamma_{yL} - \bar{\gamma}_y - \frac{\varepsilon_y |y_0| \theta_m}{\sqrt{{x_0}^2 + {y_0}^2}}}{U_\phi}\right)\right] \end{array} \right\} dx_0 dy_0, \tag{20}$$

where C_B and C_E are the instantaneous capacities of the legitimate transmission (Alice-Bob) and the wiretap channel (Alice-Eve), respectively. Unlike RF wireless communications, the transmitted signal in VLC must be unipolar and satisfy amplitude constraints to avoid clipping distortion. We consider the secrecy capacity for VLC with both average and peak optical intensity constraints. Lower and upper bounds on the secrecy capacity are derived in [7],

$$C_s \geq C_{sL} = \frac{1}{2}\log\left\{\frac{\sigma_E^2\left[h_B^2 e^{-2c\xi P}\left(\frac{e^{cA}-1}{c}\right)^2 + 2\pi e\sigma_B^2\right]}{2\pi e\sigma_B^2\left[\frac{h_E^2 A(cA-2)}{c(1-e^{-cA})} + \frac{2h_E^2}{c^2} - h_E^2\xi^2P^2 + \sigma_E^2\right]}\right\}, \tag{22}$$

$$C_s \leq C_{sU} = \frac{1}{2}\log\left\{\frac{\left(\frac{h_E^2}{h_B^2}\sigma_B^2 + \sigma_E^2\right)\left(h_B^2 A\xi P + \sigma_B^2\right)}{\sigma_B^2\left(h_E^2 A\xi P + 2\frac{h_E^2}{h_B^2}\sigma_B^2 + \sigma_E^2\right)\left(1 + \frac{h_E^2\sigma_B^2}{h_B^2\sigma_E^2}\right)}\right\}, \tag{23}$$

where A is the peak optical intensity of the LED; $\xi \in (0, 1]$ is the dimming target; $P \in (0, A]$ is the nominal optical intensity of the LED for long-term stable operation and the average optical intensity is ξP; c is the solution to equation $\frac{\xi P}{A} = \frac{1}{1-e^{-cA}} - \frac{1}{cA}$; σ_B^2 and σ_E^2 denote the variances of additive white Gaussian noise at Bob and Eve, respectively.

When Bob's channel is worse than Eve's channel (i.e., $h_B/\sigma_B < h_E/\sigma_E$), the secrecy capacity C_s is zero and secure transmission cannot be guaranteed. It is necessary to characterize the insecure region and the effects of water waves on the insecure region. In addition, SOP reflects the events that the instantaneous secrecy capacity is below target rate R_s, given by,

$$p_{out} = p\left(C_s \leq R_s\right). \tag{24}$$

Lower and upper bounds on SOP can be expressed as follows,

$$\begin{cases} p_{out} \leq p\left(C_{sL} \leq R_s\right) \\ p_{out} \geq p\left(C_{sU} \leq R_s\right) \end{cases}. \tag{25}$$

The probability of SPSC can be regarded as the probability of existence of a secure communication, written as,

$$p_s = p\left(C_s > 0\right). \tag{26}$$

Since the channel capacity C increases monotonically with the channel gain h, assuming noise variance $\sigma_B^2 = \sigma_E^2$, (26) can be rewritten as,

$$p_s = p\left(h_B > h_E\right). \tag{27}$$

III. Model Verification Via Experiments

A. Wave Slope Measurements

To verify the theoretical derivation via experiments, we need to quantitatively characterize the wave slope statistics under laboratory condition. We adopt the slope measurement system shown in Fig. 3(a) to obtain the statistics of the wave slope [20],

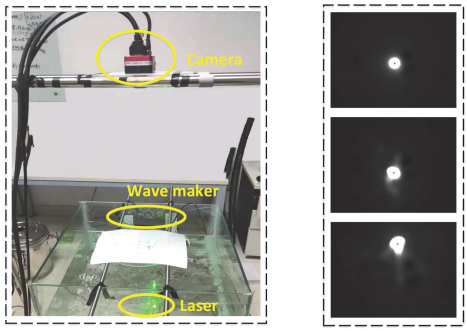

Fig. 3. (a) The experimental system of wave slope measurement and (b) the laser spot on the screen.

where a laser pointer (HMSfSYymR4x, 532 nm) is directed vertically upward through the water surface and a wave generator is placed in a water tank (Yujang CX-W3) to generate the wave. After refraction, the beam passes through a lens and falls on a screen placed at the focal plane of the lens. As the channel coherence time with water fluctuation is a few milliseconds in the experimental measurements, a camera (Flare 2M360MCL) with frame rate 400 frame/s and exposure time 400 ns is adopted to capture the laser spots on the screen. Due to dynamic water waves, the spot position of each frame fluctuates randomly, and the center coordinates of light spot are extracted through image processing, which are marked as red dots in Fig. 3(b). Then, the slope angle of the area where the narrow laser beam emerges can be obtained from x and y coordinates of the spot through geometric relations, which is described in [20], where R_x is the slope angle measured on $x-z$ plane and R_y is that on $y-z$ plane.

By recording 10,000 frames, the probability density functions (PDFs) of slope angles R_x and R_y are shown in Fig. 4. The slope mainly lies in the range of $[-40, 40]$ degrees and is symmetrically distributed around 0°, which is similar to the outdoor experimental results in [21]. Compared with Gaussian distribution, the PDF is steeper near 0 ° and thus Gaussian cannot well fit. Similar to [22], we examine the accuracy of various statistical distributions in terms of their goodness of fit to the experimental data. One-sample Kolmogorov-Smirnov (K-S) test (corresponding to k-s test function in Matlab) is adopted to test the null hypothesis where the empirical cumulative distribution function (CDF) of the data is equal to the hypothesized CDF [23]–[25]. The null hypothesis is rejected ($h = 1$) if the p-value is lower than the significance level 5%. For slope angle R_x, the results are $h = 0$ and $p = 0.17$, which indicate that logistic distribution can well fit the experimental data. Meanwhile, the hypothesis test results of normal distribution ($h = 1$, $p = 2.42 \times 10^{-10}$), extreme value distribution ($h = 1$, $p = 3.94 \times 10^{-75}$) and generalized extreme value distribution ($h = 1$, $p = 1.69 \times 10^{-30}$) show that the data cannot be well fitted by these distributions. For slope angle R_y, we have $h = 0$ and $p = 0.15$ for logistic distribution, and the hypothesis test results of normal distribution ($h = 1$, $p = 5.02 \times 10^{-7}$), extreme value distribution ($h = 1$, $p = 1.36 \times 10^{-38}$) and generalized extreme value distribution

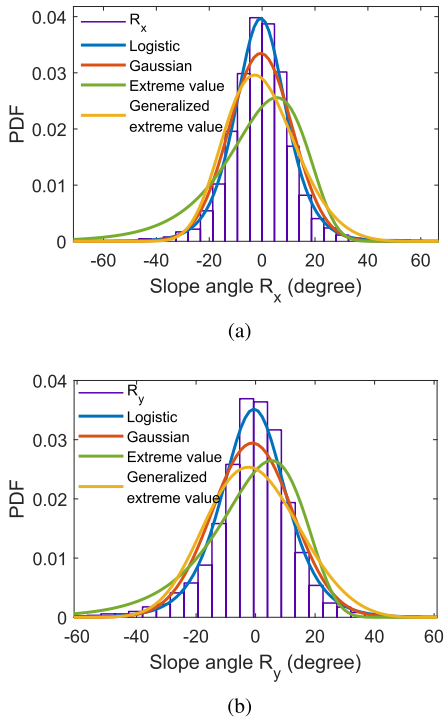

Fig. 4. The PDFs of the slope angles (a) R_x and (b) R_y.

$(h = 1, p = 3.15 \times 10^{-37})$. It is seen that the data can be well fitted by a logistic distribution with parameters u_w and σ_w, i.e.,

$$f(x) = \frac{\exp\left(\frac{x-u_w}{\sigma_w}\right)}{\sigma_w\left[1+\exp\left(\frac{x-u_w}{\sigma_w}\right)\right]^2}. \tag{28}$$

A water surface can be considered as a collection of patches and assume the same surface slope parameter within each patch scale for short-scale waves [26]. In our experimental environment, the waves in the tank can be considered as irregular short waves, and we can apply the measured PDFs of slope angles to generate random water surface in the numerical evaluation.

B. W2A-VLC System

A W2A-VLC system is established to verify the accuracy of the proposed theoretical model and investigate the secrecy performance under wavy surface, as shown in Fig. 5. The wave slope statistics is approximated by a logistic distribution shown in (28). An arbitrary waveform generator (AWG, Rigol DG5252) is adopted to generate a sinusoidal wave ($f = 50$ kHz, $V_{pp} = 3$ V) to drive a green LED (Cree XBDGRN, 520 nm) with beam angle of 43.6 degrees under depth of 0.15 m. A wave generator (Yujang CX-W3) is placed in a water tank to generate wave. Then, an avalanche photodiode (APD1, Hamamatsu C10508-01, as the legitimated receiver Bob) is placed directly above the LED at (0 m, 0 m, 0.68 m) and the received signal is sampled by a digital storage oscilloscope (DSO, Teledyne Lecroy LabMaster 10-36Zi-A) with sampling rate $f_s = 500$ kSa/s for offline signal processing. In the same way, we set the location of APD2 (Hamamatsu C10508-01) as the eavesdropper

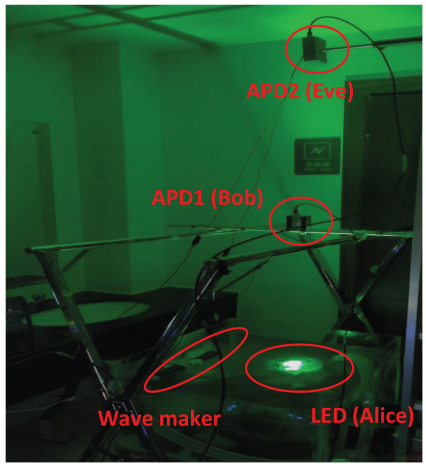

Fig. 5. The experimental system of W2A-VLC for Alice, Bob and Eve.

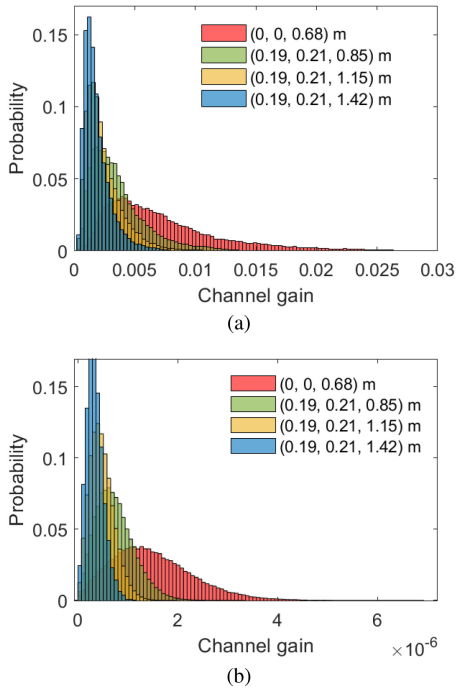

Fig. 6. The probability distributions of channel gain (a) in the experiment and (b) in the theoretical results.

Eve. Both Bob and Eve collect data under calm and wavy surface conditions. The channel gain of Bob and Eve can be extracted by using the digital signal processing method in [27]. Besides, due to different responses of the two APDs, we normalize them via the amplitudes of the same LED under the same distance to obtain an accurate ratio of channel gain.

To verify the theoretical model, we apply the statistical distribution of water waves in Fig. 4 to generate surface slopes and calculate the link gain statistics of Bob and Eve by (20). The probability distributions under wavy surface at different receiver locations in the experiment and theoretical calculation are shown in Fig. 6. It can be seen that the experimental distribution can be well fitted by that from theoretical derivations, except a scaling factor from the device amplification factors. We also compare

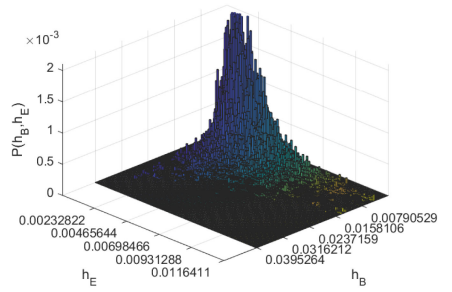

(a)

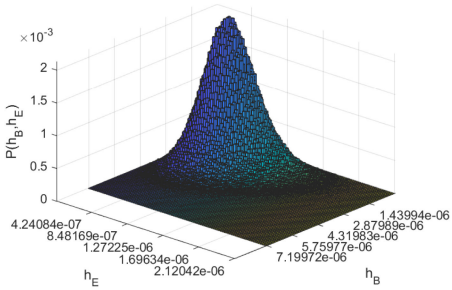

(b)

Fig. 7. The joint probability distributions of channel gain (a) in the experiment and (b) in the theoretical results.

the joint probability distribution of channel gain in Fig. 7 when Bob and Eve are located at (0 m, 0 m, 0.68 m) and (0.19 m, 0.21 m, 1.15 m), respectively. The experimental distribution is close to but not as smooth as the theoretical distribution due to noise. The scaling factor is 5.49×10^3 and the L2-norm of the difference between experimentally empirical distribution and theoretical distribution is 0.03.

Then, the secrecy performance under the given experimental condition is investigated. Fig. 8 shows ratio h_B/h_E over the time. Under calm water surface, h_B/h_E increases from 2.16 to 4.50 as Eve's elevation increases from 0.85 m to 1.42 m, and the channel gain of Bob is always larger than that of Eve. However, h_B/h_E has a large fluctuation under wavy surface and Bob's channel gain can be lower than that of Eve. The PDFs of h_B/h_E are shown in Fig. 9 for the three cases and they can be fitted by a lognormal distribution with parameters μ and σ, i.e.,

$$f(x) = \frac{1}{x\sigma\sqrt{2\pi}} \exp\left(\frac{-(\ln x - \mu)^2}{2\sigma^2}\right). \tag{29}$$

Such approximation is verified by one-sample K-S test with results $h = 0$ and $p = 0.14$.

The probability that Bob's channel is better than Eve's one can be written as,

$$\begin{aligned} p\left(h_B/h_E > 1\right) &= 1 - p\left(h_B/h_E \le 1\right) \\ &= \tfrac{1}{2} - \tfrac{1}{2} erf\left(\tfrac{-\mu}{\sqrt{2}\sigma}\right) \end{aligned}. \tag{30}$$

As Eve changes the location from (0.19 m, 0.21 m, 0.85 m) to (0.19 m, 0.21 m, 1.15 m) and (0.19 m, 0.21 m, 1.42 m), parameter μ of the lognormal distribution increases from 0.68 to 1.36 while parameter σ decreases from 0.88 to 0.73, and the probability of SPSC calculated from (30) via lognormal approximation are 78.02%, 90.59% and 96.88%, respectively, which is approximately consistent with that calculated from the raw experimental data (78.00%, 90.39% and 96.18%). It is seen that the theoretical results on the ratio distribution in Fig. 10 are similar to the experimental results in Fig. 9. The probability of SPSC at (0.19 m, 0.21 m, 0.85 m), (0.19 m, 0.21 m, 1.15 m) and (0.19 m, 0.21 m, 1.42 m) are 79.43%, 89.86% and 94.46%, respectively.

In summary, by measuring the wave slope statistics in the laboratory experimental environment, we generate the wave slopes that follow the experimental slope distribution and substitute them into (20) to calculate the channel gains. Both the channel gain distributions and the probability of SPSC obtained from experimental results are in good agreement with the theoretical results, which verify the feasibility of the theoretical calculation.

IV. Further Exploration of Secrecy Performance

After verifying the theoretical model, we further investigate the secrecy performance via numerical simulation for a wider range of parameters. Assume a collimated illuminating source with wavelength 520 nm is perpendicular to the water surface with transmission optical power $P_t = 1$ W. Assume absorption coefficient a and scattering coefficient s are 0.04 /m and 0.06 /m, respectively, close to Jerlov type IB water in [28]. The refractive index of air n' and water n are 1 and 1.33, respectively.

A. Distributions of Light Intensity and Channel Gain

We consider the calm surface in Fig. 11(a), the wavy surface whose slope satisfies sinusoidal function (peak angle of 44.7 degrees) in Fig. 11(b), and the wavy surface whose slope follows truncated logistic distribution ($u_w = 0$ degree and $\sigma_w = 5$ degrees) in the interval of $[-45$ degrees, 45 degrees], as shown in Fig. 11(c). When the depth of the source is 2 m and the elevation of the receiving plane is 1 m, the coverage and intensity distribution of light spot under calm and wavy surface conditions are shown in Fig. 12. The total receiving power on the receiving plane is 0.9679 W. Compared with the circular light spot under calm surface condition in Fig. 12(a), the light spots in Fig. 12(b) and (c) are twisted, and the intensity varies significantly from point to point.

The PDFs of channel gain at different positions are calculated from (20) when the wave slope follows truncated logistic distribution ($u_w = 0$ degree and $\sigma_w = 5$ degrees). Assume that the receiving aperture is 0.04 m. As shown by Fig. 13, the PDF gradually shifts to the left and concentrates as the receiver's height and horizontal distance increase. As the receiver moves far away from the light source, both the channel gain and the channel gain fluctuation caused by the wave are reduced.

In Fig. 14(a), the correlation coefficient between Bob's and Eve's channel is calculated. Assume Bob is at (0.1 m, 0.1 m, 1 m) and Eve's coordinate varies from (0.1 m, 0.1 m, 1 m) to (0.1 m, 0.1 m, 7 m). In case 1, the wave slope follows truncated logistic distribution ($u_w = 0$ degree and $\sigma_w = 5$ degree), divergence half-angle α of LED is 0°, underwater scattering coefficient s is 0.06 /m and wavelength λ is 520 nm. As the divergence angle increases to 10 degrees (case 2) or the scattering coefficient

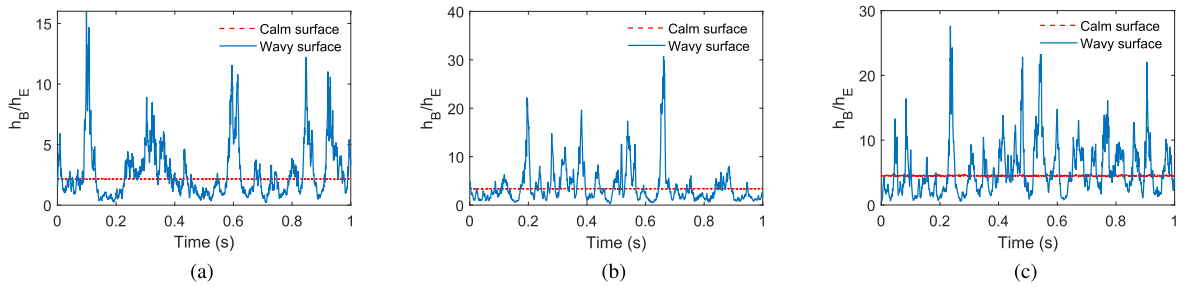

Fig. 8. The link gain h_B/h_E versus time when Eve is at (a) (0.19 m, 0.21 m, 0.85 m), (b) (0.19 m, 0.21 m, 1.15 m), and (c) (0.19 m, 0.21 m, 1.42 m) in the experiment.

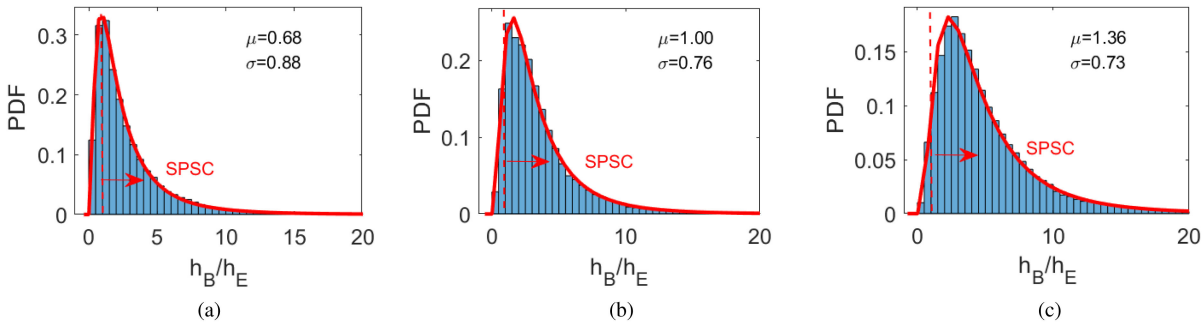

Fig. 9. The PDFs of h_B/h_E when Eve is at (a) (0.19 m, 0.21 m, 0.85 m), (b) (0.19 m, 0.21 m, 1.15 m) and (c) (0.19 m, 0.21 m, 1.42 m) in the experiment.

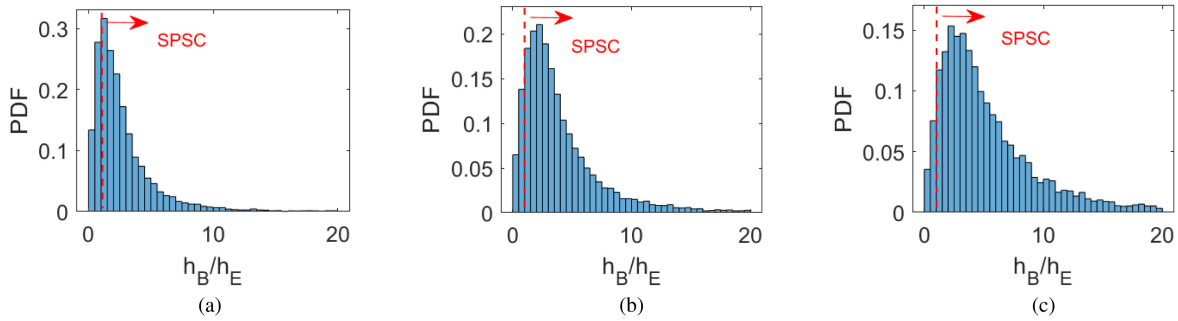

Fig. 10. The PDFs of h_B/h_E when Eve is at (a) (0.19 m, 0.21 m, 0.85 m), (b) (0.19 m, 0.21 m, 1.15 m) and (c) (0.19 m, 0.21 m, 1.42 m) in the theoretical results.

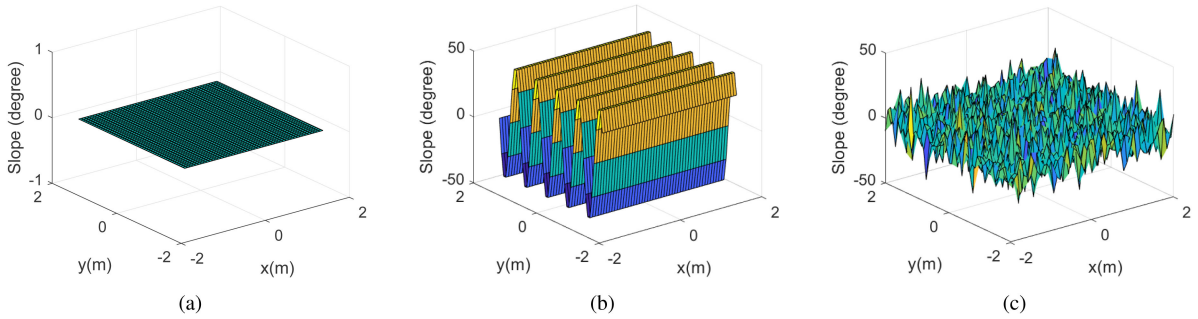

Fig. 11. Slopes of (a) calm surface, (b) wavy surface (sinusoidal function) and (c) wavy surface (truncated logistic distribution).

increases to 0.08 /m (case 3) or the wavelength decreases to 310 nm (case 4), the correlation is enhanced, which is similar in Fig. 14(b). The reason is that a light with a shorter wavelength has a larger scattering coefficient, and increasing scattering or divergence can reduce the channel gain fluctuations. Fig. 14(b) shows the correlation coefficient with respect to x-coordinate of Eve (from (0.1 m, 0.1 m, 1 m) to (0.2 m, 0.2 m, 1 m)). Compared with Fig. 14(a), the correlation coefficient decreases more rapidly with horizontal distance, which means horizontal displacement causes greater difference in terms of light intensity.

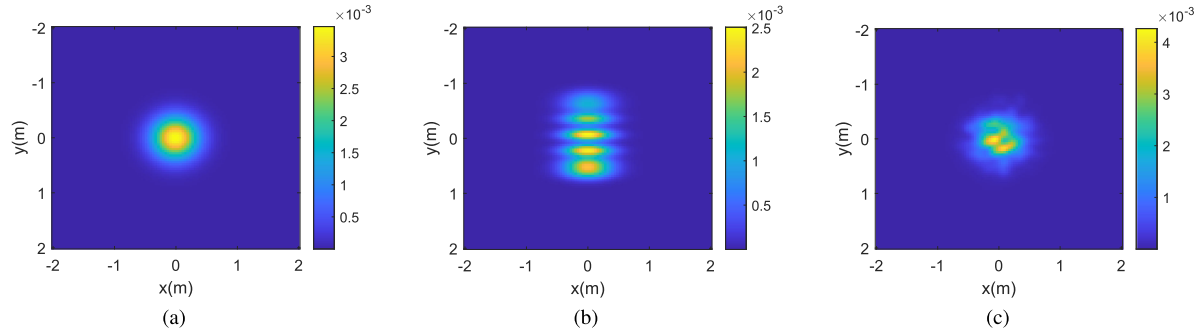

Fig. 12. The intensity distributions of light spot on the receiving plane for (a) calm surface, (b) wavy surface (sinusoidal function) and (c) wavy surface (truncated logistic distribution).

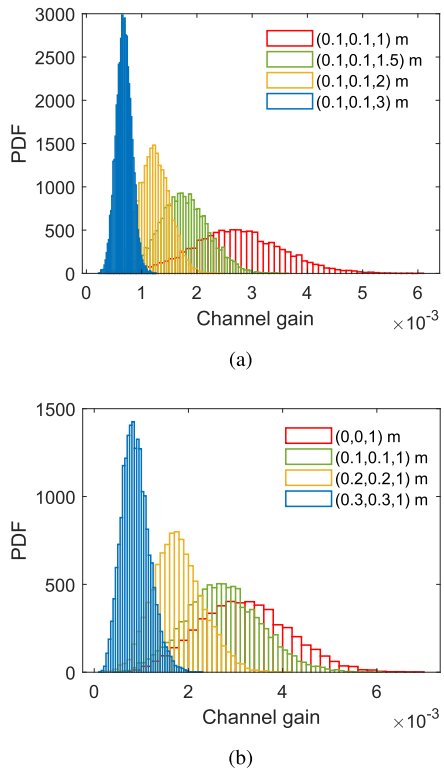

Fig. 13. Channel gain distributions (a) versus different elevations (z-coordinate) and (b) versus different horizontal positions (x-coordinate and y-coordinate).

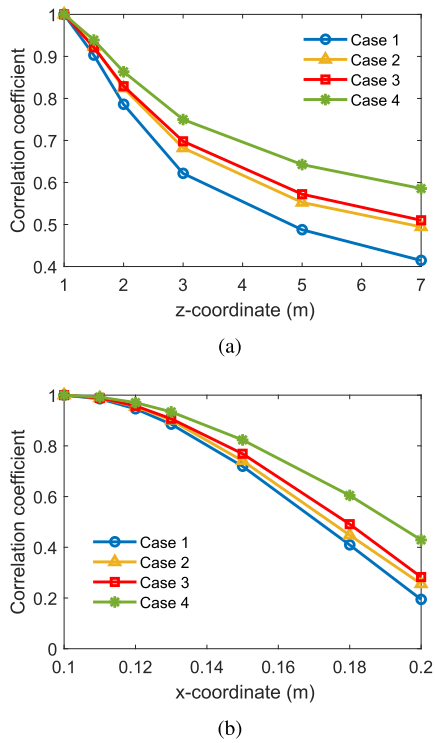

Fig. 14. Correlation coefficients (a) versus different z-coordinate of Eve (x = 0.1 m, y = 0.1 m) and (b) versus x-coordinate of Eve (x = y, z = 1 m) under case 1 ($\sigma_w = 5$ degrees, $\alpha = 0$ degree, $s = 0.06$ /m, $\lambda = 520$ nm), case 2 ($\sigma_w = 5$ degrees, $\alpha = 10$ degrees, $s = 0.06$ /m, $\lambda = 520$ nm), case 3 ($\sigma_w = 5$ degrees, $\alpha = 0$ degree, $s = 0.08$ /m, $\lambda = 520$ nm) and case 4 ($\sigma_w = 5$ degrees, $\alpha = 0$ degree, $s = 0.118$ /m, $\lambda = 310$ nm).

B. Insecure Region

Assume that the receiving apertures of Bob and Eve are both 0.04 m. Bob is located above the light source at (0 m, 0 m, 1 m) and Eve is located in various positions on the receiving plane with height 1 m. In the following, we assume that $\sigma_B = \sigma_E$, where the area is insecure if and only if $h_B < h_E$. Fig. 15 shows the contour line of $\log_{10}(h_B/h_E)$ versus different positions of Eve under certain time instants. Under calm surface, no area in the receiver plane belongs to insecure region, as shown in Fig. 15(a), and the secure transmission can be guaranteed for all positions on the receiver plane. When the surface is wavy, there are some insecure regions where $\log_{10}(h_B/h_E) < 0$ in Fig. 15(b) and (c). For the wave slope satisfying sinusoidal function, the insecure region consists of a series of ellipse-type areas arranged along the y-axis. When the wave slope follows truncated logistic distribution, the insecure region is twisted with irregular shape.

C. Probability of Strictly Positive Secrecy Capacity

Due to wavy water surface, Eve's channel gain can be larger than Bob' one, leading to zero secrecy capacity. In Fig. 16(a), we calculate h_B/h_E under different Eve's locations, assuming that the slope of wavy surface follows truncated logistic distribution ($u_w = 0$ degree and $\sigma_w = 5$ degrees) and Bob is at (0 m, 0 m,

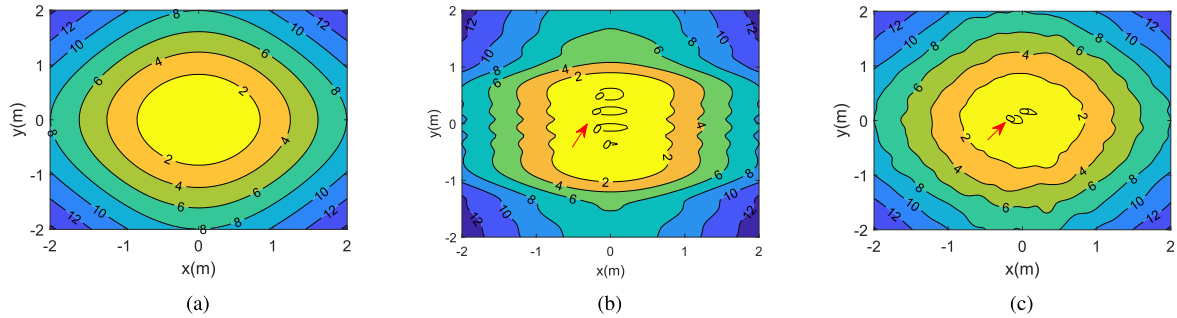

Fig. 15. $\log_{10}(h_B/h_E)$ versus different positions of Eve for the (a) calm surface, (b) wavy surface (sinusoidal function) and (c) wavy surface (truncated logistic distribution).

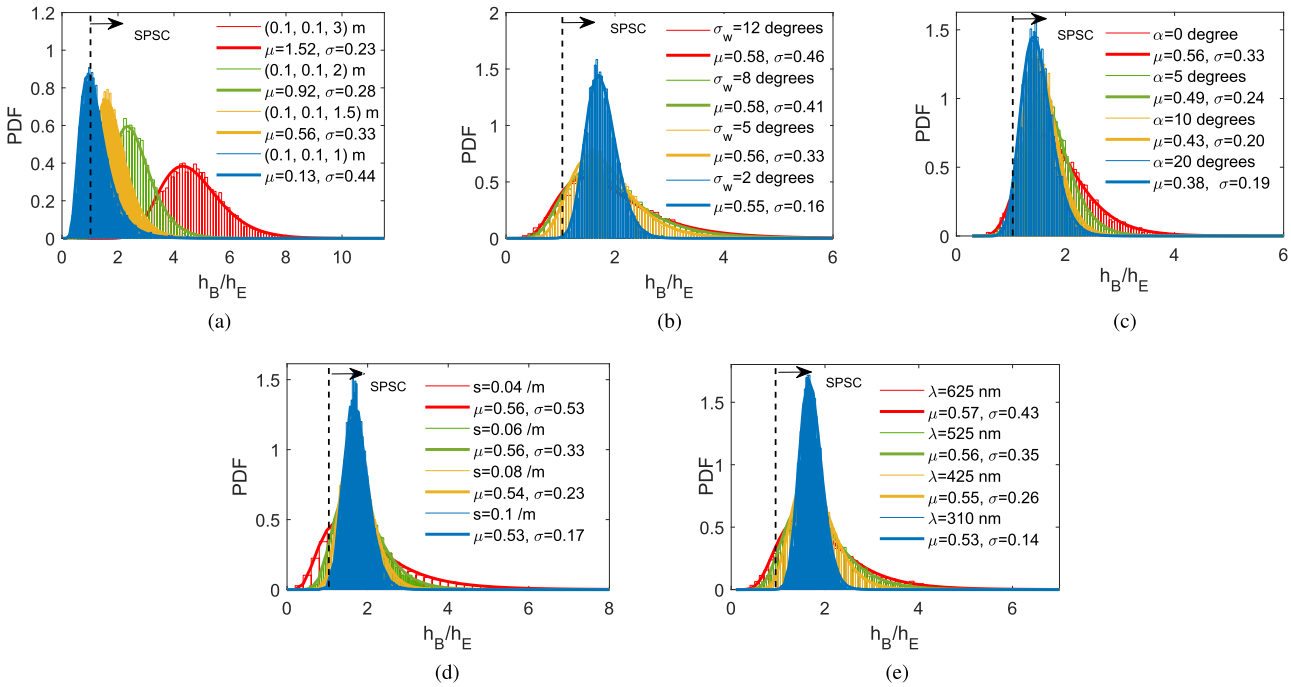

Fig. 16. The PDFs of h_B/h_E (a) for different Eve's elevations z_E ($x_E = y_E = 0.1$ m, $\sigma_w = 5$ degrees, $\alpha = 0$ degree, $s = 0.06$ /m), (b) for different σ_w of truncated logistic distribution of the wave slope ($z_E = 1.5$ m, $\alpha = 0$ degree, $s = 0.06$ /m), (c) for different initial divergence half-angles α of the LED ($z_E = 1.5$ m, $\sigma_w = 5$ degrees, $s = 0.06$ /m), (d) for different scattering coefficients s of the water ($z_E = 1.5$ m, $\sigma_w = 5$ degrees, $\alpha = 0$ degree) and (e) for different wavelengths λ of the LED ($z_E = 1.5$ m, $\sigma_w = 5$ degrees, $\alpha = 0$ degree).

1 m). Other parameters are stated in the figure caption. The PDFs can be well fitted by lognormal distributions, which is verified by the experimental result in Fig. 9.

When Eve moves away from Bob, the probability of Eve's channel gain being larger than Bob's decreases and the probability of SPSC increases from 62.66% to 100% as Eve rises from 1 m to 3 m, as shown in Fig. 16(a) and Fig. 17(a). In Fig. 16(b), as the wave intensity increases, the range of h_B/h_E becomes larger and the probability of SPSC gradually drops from 100% to 91.04% as σ_w increases to 12 degrees in Fig. 17(b). In Fig. 16(b) and Fig. 17(c), when the divergence half-angle of the LED increases from 0 degrees to 7 degrees, the probability of SPSC increases steadily from 95.50% to 98.15% and then decreases to 97.60% as the divergence half-angle increases to 20 degrees. The reason is that small beam width is susceptible to wave fluctuation and drifts out of Bob's receiving aperture, where the channel gain of Bob changes more significantly, leading to lower secrecy performance. For too large beam width, the difference in optical power received by Bob and Eve is reduced, which degrades the secrecy performance. In addition, we consider different scattering coefficients from different diameters and concentration levels of scattered particles. In Fig. 16(d), the PDF becomes concentrated as the scattering coefficient of water increases, and the probability of SPSC rises from 87.14% to 99.82% as the scattering coefficient increases from 0.04 /m to 0.1 /m in Fig. 17(d). A larger scattering coefficient results in a more divergent beam and random scattering, which can mitigate the effect of wave variation. Hence, the probability of Bob's channel being better than Eve's one increases steadily. In Fig. 16(e) and Fig. 17(e), the light beam with different wavelengths are transmitted into clear ocean water, i.e., Jerlov type IB water. The scattering coefficients and absorption coefficients corresponding

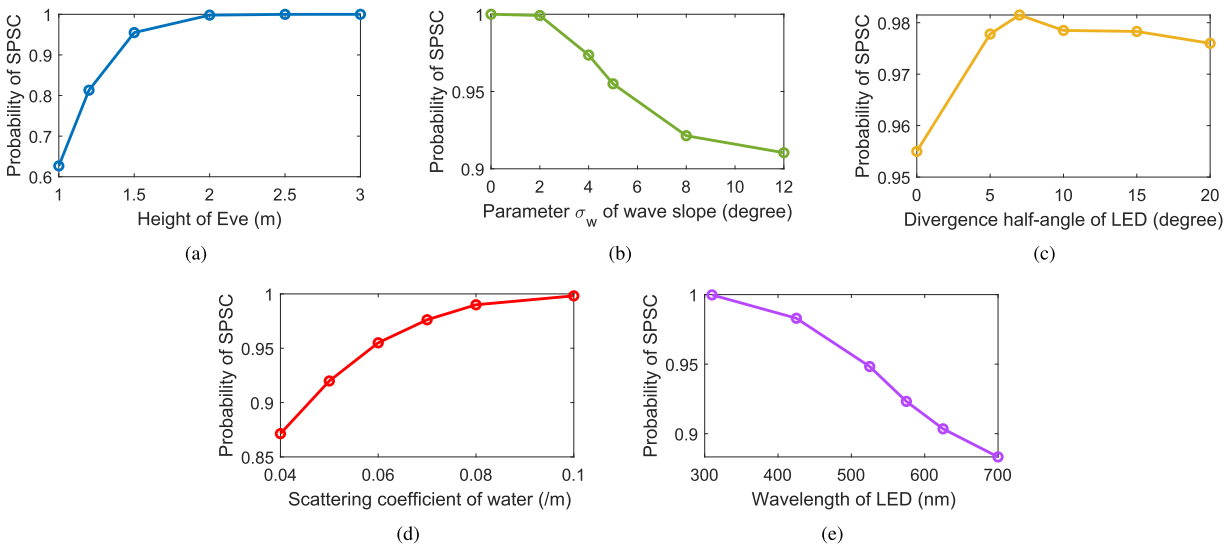

Fig. 17. The probability of SPSC versus (a) Eve's elevation z_E ($\sigma_w = 5$ degrees, $\alpha = 0$ degree, $s = 0.06$ /m), (b) parameter σ_w of wave slope ($z_E = 1.5$ m, $\alpha = 0$ degree, $s = 0.06$ /m), (c) divergence half-angle α of the LED ($z_E = 1.5$ m, $\sigma_w = 5$ degrees, $s = 0.06$ /m), (d) scattering coefficient s of the water ($z_E = 1.5$ m, $\sigma_w = 5$ degrees, $\alpha = 0$ degree) and (e) wavelength λ of the LED ($z_E = 1.5$ m, $\sigma_w = 5$ degrees, $\alpha = 0$ degree).

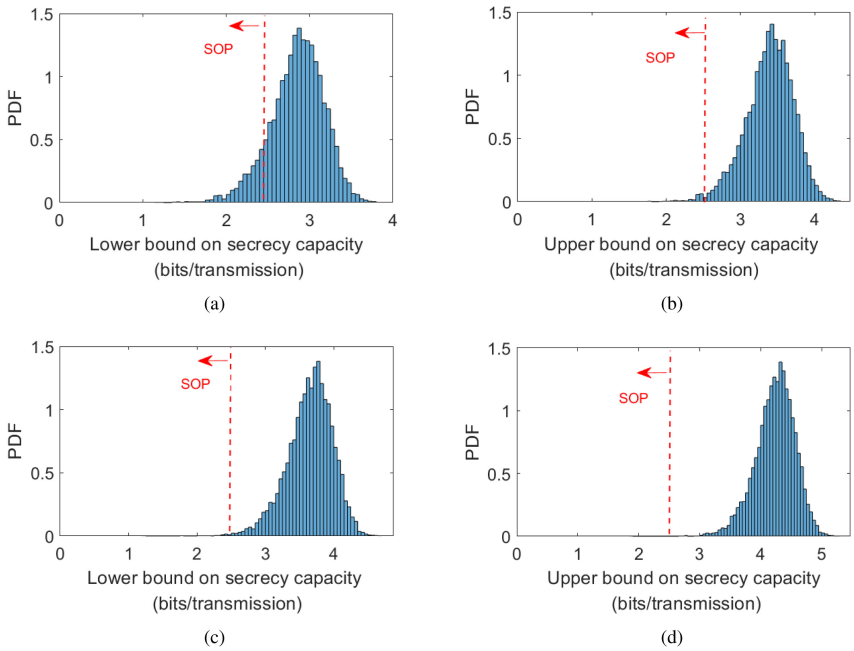

Fig. 18. The PDFs of the (a) lower bound and (b) upper bound on secrecy capacity when Eve is at (0.1 m, 0.1 m, 5 m). The PDFs of the (c) lower bound and (d) upper bound on secrecy capacity when Eve is at (0.1 m, 0.1 m, 7 m) ($\sigma_w = 5$ degrees, $\alpha = 0$ degree, $s = 0.06$ /m).

to different wavelengths can be found in [28]. Since the light with a shorter wavelength has a larger scattering coefficient, which can reduce the effect of wavy surface, the probability of SPSC decreases from 99.98 % to 88.33 % as the wavelength increases from 310 nm to 700 nm.

D. Secrecy Outage Probability

The lower and upper bounds on the secrecy capacity are calculated according to (22) and (23), respectively. Assume dimming target $\xi = 0.2$, peak optical intensity $A = P = 50$ dB, the noise variances at Bob and Eve are normalized to 1, i.e., $\sigma_B^2 = \sigma_E^2 = 1$. The slope of wavy surface follows truncated logistic distribution ($u_w = 0$ degree and $\sigma_w = 5$ degrees) and Bob is at (0 m, 0 m, 1 m). Fig. 18 shows the PDFs of lower and upper bounds when Eve is at (0.1 m, 0.1 m, 5 m) and (0.1 m, 0.1 m, 7 m). If the target secrecy rate is set to 2.5 bits/transmission, for Eve at (0.1 m, 0.1 m, 5 m), the lower and upper bounds on SOP are 1.00% and 13.37%, respectively. As Eve moves away from Bob to (0.1 m, 0.1 m, 7 m), the upper bound on SOP decreases to 0.28% and the lower bound decreases to 0.01%.

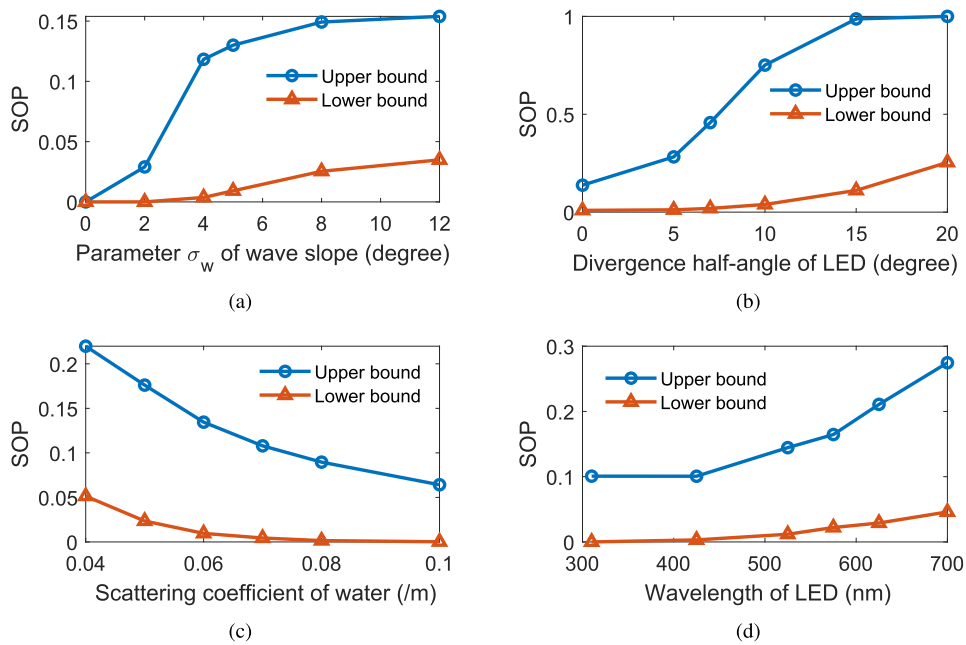

Fig. 19. The upper and lower bounds on SOP versus (a) σ_w of wave slope ($z_E = 5$ m, $\alpha = 0$ degree, $s = 0.06$ /m), (b) divergence half-angle α of the LED ($z_E = 5$ m, $\sigma_w = 5$ degrees, $s = 0.06$ /m), (c) scattering coefficients s of the water ($z_E = 5$ m, $\sigma_w = 5$ degrees, $\alpha = 0$ degree) and (d) wavelength λ of the LED ($z_E = 5$ m, $\sigma_w = 5$ degrees, $\alpha = 0$ degree).

In Fig. 19(a), as parameter σ_w of the wave slope increase from 0 to 12 degrees while Eve is at (0.1 m, 0.1 m, 5 m), the upper bound on SOP increases from 0% to 15.39% and the lower bound increases from 0% to 3.49%. The water surface fluctuation increases the probability of low secrecy rate and thus increases the outage probability. In Fig. 19(b), the optical power received by Bob decreases as the divergence half-angle of LED increases from 0 ° to 20 degrees, leading to lower secrecy rate. Therefore, the upper bound increases from 13.77% to 100% and the lower bound increases from 0.90% to 25.40%. In addition, we change the scattering coefficient of water in Fig. 19(c). It is seen that the SOP decreases with the scattering coefficient, where the upper bound decreases from 21.98% to 6.42% and the lower bound decreases from 5.14% to 0.02%, since random scattering mitigates the effect of water surface fluctuations and improves the secrecy performance. Fig. 19(d) shows that the secrecy performance degrades as the wavelength of LED increases. For Jerlov type IB water, the light with a shorter wavelength has larger scattering coefficients, which reduces the probability of low secrecy rate caused by wavy surface. The upper bound on SOP increases from 10.08% to 27.46% and the lower bound increases from 0% to 4.60%.

Finally, we investigate the impact of background light on SOP. Hamamatsu C12702 model APD (photosensitive area $1\ \mathrm{mm} \times 1\ \mathrm{mm}$) is adopted for Bob (0 m, 0 m, 1 m) and Eve (0.1 m, 0.1 m, 5 m), whose photoelectric conversion characteristic is shown in [29]. Generally, background light from the sun can be considered as a constant DC optical signal. Strong background light may shift the operating point of APD to the saturation region, causing negligible AC response [30]. Assume that the average optical power in the transmitter is adjusted to guarantee Bob's APD operating at the optimal point ($P_B = 8.51 \times 10^{-5}$ W) under calm surface, where the received optical power of Eve is $P_E = 8.38 \times 10^{-6}$ W. As the received background power of APD increases, the variation of AC response and noise is shown in Fig. (3-6) in [29]. According to such relationship, as background power increases to 1 mW, the overall channel gains of Bob and Eve both decrease to near 0, and thus the lower and upper bounds on SOP increase to 100%, as shown in Fig. 20, which indicates that strong background light significantly degrades the secrecy performance.

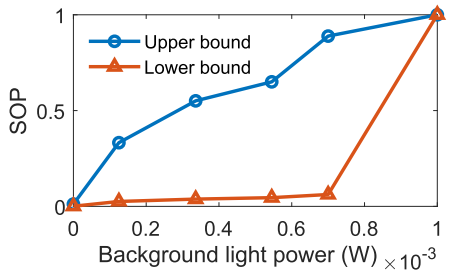

Fig. 20. The upper and lower bounds on SOP versus received background light power ($\sigma_w = 5$ degrees, $\alpha = 0$ degree, $s = 0.06$ /m).

V. Conclusion

In this work, we have investigated the secrecy performance of W2A-VLC systems. The channel gain of Bob and Eve under surface fluctuation and underwater scattering are theoretically derived. A laboratory W2A-VLC system is established to verify the theoretical model, and the experimental results show that the probability of secure communication increases from 90.39% to 96.18% as the eavesdropper's elevation increases from 1.15 m to 1.42 m, which are approximately consistent with numerical

results. The PDFs of wave slope are experimentally measured, which are approximated by logistic distributions. To investigate the parameters that affect secrecy performance, the secrecy performance metrics including insecure regions, the probability of SPSC and SOP under different wave intensities, locations, divergence angles of LED, underwater scattering coefficients and wavelengths of transmitted beam are numerically investigated. It is seen that water surface fluctuations can cause information leakage while underwater scattering can mitigate the effect of dynamic waves and improve the secrecy performance.

Appendix A
Proof of (16)

From (15), we can obtain γ_x and γ_y, given by,

$$\gamma_x = \arctan\left(\frac{\left(n'\sqrt{b_1}+b_2\right)\tan\left(\gamma'_x\right)-b_3\tan\left(R_x\right)}{n'\sqrt{b_1}+b_2-b_3}\right), \tag{31}$$

$$\gamma_y = \arctan\left(\frac{\left(n'\sqrt{b_1}+b_2\right)\tan\left(\gamma'_y\right)-b_3\tan\left(R_y\right)}{n'\sqrt{b_1}+b_2-b_3}\right), \tag{32}$$

where

$$\begin{aligned} b_1 = &\left(n^2-n'^2\right)\left(\tan^2\left(\gamma'_x\right)+\tan^2\left(\gamma'_y\right)\right.\\ &\left.+\tan^2\left(R_x\right)+\tan^2\left(R_y\right)\right)\\ &+n^2+n^2\left(\tan^2\left(\gamma'_x\right)+\tan^2\left(\gamma'_y\right)\right)\left(\tan^2\left(R_x\right)\right.\\ &\left.+\tan^2\left(R_y\right)\right)\\ &+2n'^2\left(\tan\left(\gamma'_x\right)\tan\left(R_x\right)+\tan\left(\gamma'_y\right)\tan\left(R_y\right)\right)\\ &-n'^2\left(\tan\left(\gamma'_x\right)\tan\left(R_y\right)-\tan\left(\gamma'_y\right)\tan\left(R_x\right)\right)^2, \end{aligned} \tag{33}$$

$$b_2 = n'^2\left(\tan\left(\gamma'_x\right)\tan\left(R_x\right)+\tan\left(\gamma'_y\right)\tan\left(R_y\right)+1\right), \tag{34}$$

$$b_3 = \left(n'^2-n^2\right)\left(\tan^2\left(\gamma'_x\right)+\tan^2\left(\gamma'_y\right)+1\right), \tag{35}$$

and R_x is the angle between the projection line of slope and the z axis in the $x-z$ plane, while R_y is the angle on $y-z$ plane. Therefore, the maximum and minimum incident angles can be given by,

$$\begin{cases} [\gamma_{xL},\gamma_{xU}] = [\min(\gamma_x),\max(\gamma_x)] \\ [\gamma_{yL},\gamma_{yU}] = [\min(\gamma_y),\max(\gamma_y)] \end{cases}. \tag{36}$$

Appendix B
Proof of (20)

For simplicity of notation, we define variables c_1 and c_2, and (1) can be written as,

$$\begin{aligned} &\Delta I\left(x_0,y_0,z_0,\gamma_x,\gamma_y\right)\\ &=\frac{P_t}{\left(\pi U_\phi R_1\right)^2}\exp\left\{\begin{array}{l}-a\sqrt{\left({x_0}^2+{y_0}^2+{z_0}^2\right)}-\frac{{\xi_x}^2+{\xi_y}^2}{{R_1}^2}\\ -\frac{1}{{U_\phi}^2}\left[\left(\gamma_x-c_1\right)^2+\left(\gamma_y-c_2\right)^2\right]\end{array}\right\}\\ &=\frac{P_t}{\left(\pi U_\phi R_1\right)^2}\exp\left\{\begin{array}{l}-a\sqrt{\left({x_0}^2+{y_0}^2+{z_0}^2\right)}-\frac{{\xi_x}^2+{\xi_y}^2}{{R_1}^2}\\ -\frac{1}{{U_\phi}^2}\left({c_1}^2+{c_2}^2\right)\end{array}\right\}\\ &\quad\times\exp\left\{-\frac{1}{{U_\phi}^2}\left({\gamma_x}^2+{\gamma_y}^2-2c_1\gamma_x-2c_2\gamma_y\right)\right\}, \end{aligned} \tag{37}$$

where

$$c_1 = \bar{\gamma}_x+\frac{\varepsilon_x\left|x_0\right|\theta_m}{\sqrt{{x_0}^2+{y_0}^2}}, \tag{38}$$

$$c_2 = \bar{\gamma}_y+\frac{\varepsilon_y\left|y_0\right|\theta_m}{\sqrt{{x_0}^2+{y_0}^2}}. \tag{39}$$

Then, the integral of (37) over γ_x and γ_y is given by,

$$\begin{aligned} &\int_{\gamma_x}\int_{\gamma_y}\Delta I\left(x_0,y_0,z_0,\gamma_x,\gamma_y\right)d\gamma_x d\gamma_y\\ &=\int_{\gamma_x}\int_{\gamma_y}c_3\exp\left\{-\frac{1}{{U_\phi}^2}\left({\gamma_x}^2+{\gamma_y}^2-2c_1\gamma_x-2c_2\gamma_y\right)\right\}d\gamma_x d\gamma_y\\ &=c_3\int_{\gamma_x}\exp\left\{-\frac{1}{{U_\phi}^2}{\gamma_x}^2+\frac{2c_1}{{U_\phi}^2}\gamma_x\right\}d\gamma_x\times\\ &\quad\int_{\gamma_y}\exp\left\{-\frac{1}{{U_\phi}^2}{\gamma_y}^2+\frac{2c_2}{{U_\phi}^2}\gamma_y\right\}d\gamma_y, \end{aligned} \tag{40}$$

where

$$\begin{aligned} c_3 = &\frac{P_t}{\left(\pi U_\phi R_1\right)^2}\exp\left\{-a\sqrt{\left({x_0}^2+{y_0}^2+{z_0}^2\right)}-\frac{{\xi_x}^2+{\xi_y}^2}{{R_1}^2}\right\}\\ &\times\exp\left\{-\frac{1}{{U_\phi}^2}\left[{c_1}^2+{c_2}^2\right]\right\}. \end{aligned} \tag{41}$$

One integral term in (40) can be rewritten as,

$$\begin{aligned} &\int_{\gamma_x}\exp\left\{-\frac{1}{{U_\phi}^2}{\gamma_x}^2+\frac{2c_1}{{U_\phi}^2}\gamma_x\right\}d\gamma_x\\ &=\mathrm{e}^{\frac{{c_1}^2}{{U_\phi}^2}}\int_{\gamma_{xL}}^{\gamma_{xU}}\exp\left\{-\frac{\left(\gamma_x-c_1\right)^2}{{U_\phi}^2}\right\}d\gamma_x\\ &\overset{t_1=\gamma_x-c_1}{=\!=\!=\!\Rightarrow}\mathrm{e}^{\frac{{c_1}^2}{{U_\phi}^2}}\int_{\gamma_{xL}-c_1}^{\gamma_{xU}-c_1}\exp\left\{-\frac{{t_1}^2}{{U_\phi}^2}\right\}dt_1\\ &\overset{t_2=t_1/U_\phi}{=\!=\!=\!\Rightarrow}\mathrm{e}^{\frac{{c_1}^2}{{U_\phi}^2}}\times U_\phi\times\frac{\sqrt{\pi}}{2}\int_{(\gamma_{xL}-c_1)/U_\phi}^{(\gamma_{xU}-c_1)/U_\phi}\frac{2}{\sqrt{\pi}}\exp\left\{-{t_2}^2\right\}dt_2\\ &=\mathrm{e}^{\frac{{c_1}^2}{{U_\phi}^2}}\times U_\phi\times\frac{\sqrt{\pi}}{2}\left[erf\left(\frac{\gamma_{xU}-c_1}{U_\phi}\right)-erf\left(\frac{\gamma_{xL}-c_1}{U_\phi}\right)\right]. \end{aligned} \tag{42}$$

Similarly,

$$\begin{aligned} &\int_{\gamma_y}\exp\left\{-\frac{1}{{U_\phi}^2}{\gamma_y}^2+\frac{2c_2}{{U_\phi}^2}\gamma_y\right\}d\gamma_y\\ &=\mathrm{e}^{\frac{{c_2}^2}{{U_\phi}^2}}U_\phi\frac{\sqrt{\pi}}{2}\left[erf\left(\frac{1}{U_\phi}\left(\gamma_{yU}-c_2\right)\right)-erf\left(\frac{1}{U_\phi}\left(\gamma_{yL}-c_2\right)\right)\right]. \end{aligned} \tag{43}$$

Therefore, (40) can be rewritten as,

$$\begin{aligned}&\int_{\gamma_x}\int_{\gamma_y}\Delta I\left(x_0,y_0,z_0,\gamma_x,\gamma_y\right)d\gamma_x d\gamma_y\\&=\frac{P_t}{4\pi {R_1}^2}\exp\left\{-a\sqrt{({x_0}^2+{y_0}^2+{z_0}^2)}-\frac{{\xi_x}^2+{\xi_y}^2}{{R_1}^2}\right\}\times\\&\left[erf\left(\frac{\gamma_{xU}-c_1}{U_\phi}\right)-erf\left(\frac{\gamma_{xL}-c_1}{U_\phi}\right)\right]\times\\&\left[erf\left(\frac{\gamma_{yU}-c_2}{U_\phi}\right)-erf\left(\frac{\gamma_{yL}-c_2}{U_\phi}\right)\right].\end{aligned}\tag{44}$$

$$\begin{aligned}h&=\frac{1}{p_t}\int_{x_0}\int_{y_0}\int_{\gamma_x}\int_{\gamma_y}\Delta I\left(x_0,y_0,z_0,\gamma_x,\gamma_y\right)d\gamma_x d\gamma_y dx_0 dy_0\\&=\\&\int_{x_0}\int_{y_0}\left\{\begin{array}{l}\frac{1}{4\pi {R_1}^2}\exp\left\{-a\sqrt{({x_0}^2+{y_0}^2+{z_0}^2)}-\frac{{\xi_x}^2+{\xi_y}^2}{{R_1}^2}\right\}\times\\\left[erf\left(\frac{\gamma_{xU}-\bar{\gamma}_x-\frac{\varepsilon_x|x_0|\theta_m}{\sqrt{{x_0}^2+{y_0}^2}}}{U_\phi}\right)-erf\left(\frac{\gamma_{xL}-\bar{\gamma}_x-\frac{\varepsilon_x|x_0|\theta_m}{\sqrt{{x_0}^2+{y_0}^2}}}{U_\phi}\right)\right]\\\times\left[erf\left(\frac{\gamma_{yU}-\bar{\gamma}_y-\frac{\varepsilon_y|y_0|\theta_m}{\sqrt{{x_0}^2+{y_0}^2}}}{U_\phi}\right)-erf\left(\frac{\gamma_{yL}-\bar{\gamma}_y-\frac{\varepsilon_y|y_0|\theta_m}{\sqrt{{x_0}^2+{y_0}^2}}}{U_\phi}\right)\right]\end{array}\right\}dx_0dy_0.\end{aligned}\tag{45}$$

By substituting c_1 and c_2 in (44) shown at the top of this page, the channel gain is obtained in (45) shown at the top of this page.

REFERENCES

[1] Z. Zeng, S. Fu, H. Zhang, Y. Dong, and J. Cheng, "A survey of underwater optical wireless communications," *IEEE Commun. Surveys Tuts.*, vol. 19, no. 1, pp. 204–238, Jan.–Mar. 2017.

[2] T. Lin, C. Gong, J. Luo, and Z. Xu, "Dynamic optical wireless communication channel characterization through air-water interface," in *Proc. IEEE/CIC Int. Conf. Commun. China Workshops*, 2020, pp. 173–178.

[3] J. A. Simpson, B. L. Hughes, and J. F. Muth, "Smart transmitters and receivers for underwater free-space optical communication," *IEEE J. Sel. Areas Commun.*, vol. 30, no. 5, pp. 964–974, Jun. 2012.

[4] M. Obeed, A. M. Salhab, M.-S. Alouini, and S. A. Zummo, "Survey on physical layer security in optical wireless communication systems," in *Proc. IEEE 7th Int. Conf. Commun. Netw.*, 2018, pp. 1–5.

[5] S. Cho, G. Chen, and J. P. Coon, "Physical layer security in visible light communication systems with randomly located colluding eavesdroppers," *IEEE Wireless Commun. Lett.*, vol. 7, no. 5, pp. 768–771, Oct. 2018.

[6] G. Pan, J. Ye, and Z. Ding, "Secure hybrid VLC-RF systems with light energy harvesting," *IEEE Trans. Commun.*, vol. 65, no. 10, pp. 4348–4359, Oct. 2017.

[7] J.-Y. Wang, C. Liu, J.-B. Wang, Y. Wu, M. Lin, and J. Cheng, "Physical-layer security for indoor visible light communications: Secrecy capacity analysis," *IEEE Trans. Commun.*, vol. 66, no. 12, pp. 6423–6436, Dec. 2018.

[8] A. Mostafa and L. Lampe, "Physical-layer security for MISO visible light communication channels," *IEEE J. Sel. Areas Commun.*, vol. 33, no. 9, pp. 1806–1818, Sep. 2015.

[9] S. Cho, G. Chen, and J. P. Coon, "Securing visible light communication systems by beamforming in the presence of randomly distributed eavesdroppers," *IEEE Trans. Wireless Commun.*, vol. 17, no. 5, pp. 2918–2931, May 2018.

[10] S. Liang, Z. Fang, G. Sun, and J. Zhang, "A physical layer security approach based on optical beamforming for indoor visible light communication," *IEEE Commun. Lett.*, vol. 24, no. 10, pp. 2109–2113, Oct. 2020.

[11] S. Cho, G. Chen, and J. P. Coon, "Enhancement of physical layer security with simultaneous beamforming and jamming for visible light communication systems," *IEEE Trans. Inf. Forensics Secur.*, vol. 14, no. 10, pp. 2633–2648, Oct. 2019.

[12] F. Yang, K. Zhang, Y. Zhai, J. Quan, and Y. Dong, "Artificial noise design in time domain for indoor SISO DCO-OFDM VLC wiretap systems," *J. Lightw. Technol.*, vol. 39, no. 20, pp. 6450–6458, 2021.

[13] P. V. Trinh, A. Carrasco-Casado, A. T. Pham, and M. Toyoshima, "Secrecy analysis of FSO systems considering misalignments and eavesdropper's location," *IEEE Trans. Commun.*, vol. 68, no. 12, pp. 7810–7823, Dec. 2020.

[14] R. Boluda-Ruiz, S. C. Tokgoz, A. García-Zambrana, and K. Qaraqe, "Enhancing secrecy capacity in FSO links via MISO systems through turbulence-induced fading channels with misalignment errors," *IEEE Photon. J.*, vol. 12, no. 4, Aug. 2020, Art. no. 7903313.

[15] F. J. Lopez-Martinez, G. Gomez, and J. M. Garrido-Balsells, "Physical-layer security in free-space optical communications," *IEEE Photon. J.*, vol. 7, no. 2, Apr. 2015, Art. no. 7901014.

[16] Y. Ai, A. Mathur, G. D. Verma, L. Kong, and M. Cheffena, "Comprehensive physical layer security analysis of FSO communications over Málaga channels," *IEEE Photon. J.*, vol. 12, no. 6, Dec. 2020, Art. no. 7906617.

[17] P. Nabavi, A. S. Haq, and M. Yuksel, "Empirical modeling and analysis of water-to-air optical wireless communication channels," in *Proc. IEEE Int. Conf. Commun. Workshops*, 2019, pp. 1–6.

[18] S. Karp, "Optical communications between underwater and above surface (satellite) terminals," *IEEE Trans. Commun.*, vol. 24, no. 1, pp. 66–81, Jan. 1976.

[19] M. Bloch, J. Barros, M. R. Rodrigues, and S. W. McLaughlin, "Wireless information-theoretic security," *IEEE Trans. Inf. Theory*, vol. 54, no. 6, pp. 2515–2534, Jun. 2008.

[20] B. Hughes, H. Grant, and R. Chappell, "A fast response surface-wave slope meter and measured wind-wave moments," *Deep Sea Res.*, vol. 24, no. 12, pp. 1211–1223, 1977.

[21] J. A. Shaw and J. H. Churnside, "Scanning-laser glint measurements of sea-surface slope statistics," *Appl. Opt.*, vol. 36, no. 18, pp. 4202–4213, 1997.

[22] M. V. Jamali *et al.*, "Statistical studies of fading in underwater wireless optical channels in the presence of air bubble, temperature, and salinity random variations," *IEEE Trans. Commun.*, vol. 66, no. 10, pp. 4706–4723, Oct. 2018.

[23] L. H. Miller, "Table of percentage points of Kolmogorov statistics," *J. Amer. Stat. Assoc.*, vol. 51, no. 273, pp. 111–121, 1956.

[24] F. J. Massey, "The Kolmogorov-Smirnov test for goodness of fit," *J. Amer. Stat. Assoc.*, vol. 46, no. 253, pp. 68–78, 1951.

[25] G. Marsaglia, W. W. Tsang, and J. Wang, "Evaluating Kolmogorov's distribution," *J. Stat. Softw.*, vol. 8, no. 18, pp. 1–4, 2003.

[26] B. Chapron, V. Kerbaol, D. Vandemark, and T. Elfouhaily, "Importance of peakedness in sea surface slope measurements and applications," *J. Geophys. Rese.: Oceans*, vol. 105, no. C7, pp. 17195–17202, 2000.

[27] T. Lin, N. Huang, C. Gong, J. Luo, and Z. Xu, "Preliminary characterization of coverage for water-to-air visible light communication through wavy water surface," *IEEE Photon. J.*, vol. 13, no. 1, Feb. 2021, Art. no. 7901013.

[28] M. G. Solonenko and C. D. Mobley, "Inherent optical properties of Jerlov water types," *Appl. Opt.*, vol. 54, no. 17, pp. 5392–5401, 2015.

[29] X. Liu, C. Gong, D. Zou, Z. Babar, Z. Xu, and L. Hanzo, "Signal characterization and achievable transmission rate of VLC under receiver nonlinearity," *IEEE Access*, vol. 7, pp. 137030–137039, 2019.

[30] N. Huang, C. Gong, C. Fu, T. Wei, and Z. Xu, "Preliminary investigation of air-to-water visible light communication link under strong ambient light," in *Proc. IEEE 94th Veh. Technol. Conf.*, 2021, pp. 1–5.

Qingqing Hu received the B.S. degree from the Dalian University of Technology, Dalian, China, in 2016, the M.S. degree in 2019 from the University of Science and Technology of China, Hefei, China, where she is currently working toward the Ph.D. degree. Her research interests include physical layer security, signal processing, and water to air visible light communication.

Chen Gong (Senior Member, IEEE) received the B.S. degree in electrical engineering and mathematics (minor) from Shanghai Jiaotong University, Shanghai, China, in 2005, the M.S. degree in electrical engineering from Tsinghua University, Beijing, China, in 2008, and the Ph.D. degree from Columbia University, New York, NY, USA, in 2012. From 2012 to 2013, he was a Senior Systems Engineer with the Qualcomm Research, San Diego, CA, USA. He is currently a Faculty Member with the University of Science and Technology of China. His research interests include wireless communications, optical wireless communications, and signal processing. He was selected by the Young 1000 Talent Program of China Government in 2014. He was awarded by Hongkong Qiushi Outstanding Young Researcher Award in 2016.

Tianrui Lin received the B.S. degree from the University of Electronic Science and Technology of China, Chengdu, China, in 2019. He is currently working toward the Ph.D. degree with the Optical Wireless Communication, University of Science and Technology of China, Hefei, China. His research interests include water to air visible light communication and MIMO communication.

Jianghua Luo received the B.S. degree from Hubei University, Wuhan, China, and the M.S. and Ph.D. degrees from the Huazhong University of Science and Technology, Wuhan, China, in 2014. He is currently a Faculty Member with the Yangtze University of China, Jingzhou, China. His research interests include ultrafast optics, optoelectronic device, and optical wireless communications.

Zhengyuan Xu (Senior Member, IEEE) received the B.S. and M.S. degrees from Tsinghua University, Beijing, China, and the Ph.D. degree from the Stevens Institute of Technology, Hoboken, NJ USA. He was a tenured Full Professor with the University of California at Riverside, Riverside, CA, USA, and later with Tsinghua University, before he joined the University of Science and Technology of China, Hefei, China. He was the Founding Director of the multi-campus Center for Ubiquitous Communication by Light, University of California, and Founding Director of Wireless-Optical Communications Key Laboratory, Chinese Academy of Sciences, Beijing, China. He was a Distinguished Expert and the Chief Scientist of the National Key Basic Research Program of China. His research interests include Petahertz communications, optical wireless communications, mobile networking, artificial intelligence, wireless big data, sensing, ranging, and localization. He has authored or coauthored 400 international journal and conference papers, and coauthored a book titled *Visible Light Communications: Modulation and Signal Processing*, which has been selected by the IEEE Series on Digital & Mobile Communication and published by Wiley-IEEE Press. Since 2014, he has been on the Elsevier annual list of Most Cited Chinese Researchers. He was an Associate Editor for different IEEE/OSA journals and was a Founding Co-Chair of the IEEE Workshop on Optical Wireless Communications in 2010.